nature physics

Article

https://doi.org/10.1038/s41567-025-03108-z

Observation of a hidden charge density wave liquid

Received: 5 June 2025

Accepted: 22 October 2025

Published online: 30 December 2025

Check for updates

Joshua S. H. Lee[1,3], Thomas M. Sutter[1,3], Goran Karapetrov[2], Pietro Musumeci[1] & Anshul Kogar[1]

Charge density waves, electronic crystals that form within a host solid, have long been theorized to melt into a spatially textured electronic liquid. Although such liquid charge density waves have not been previously observed, they may be central to the phase diagrams of correlated electron systems, including high-temperature superconductors and quantum Hall states. In 1T-TaS_2, a promising material for hosting a liquid charge density wave, a structural phase transition hinders observation. Here we use femtosecond light pulses to bypass this transition, revealing how topological defect dynamics govern hidden charge density wave correlations. Following photoexcitation, charge density wave diffraction peaks broaden azimuthally, indicating the emergence of a hexatic state. At elevated temperatures, photoexcitation fully destroys both translational and orientational orders, leaving only a ring of diffuse scattering—the hallmark of a liquid charge density wave. These findings offer compelling evidence for a defect-unbinding transition to a charge density wave liquid. More broadly, this approach demonstrates a route to uncover electronic phases obscured by intervening transitions in thermal equilibrium.

An intervening phase transition can render regions of a system's thermodynamic phase space inaccessible and complicate the experimental realization of quantum phases. Trapping gases in a metastable state to avoid solidification was key to observing Bose–Einstein condensation, a hallmark achievement of twentieth century physics[1,2]. On the other hand, liquid superconductors remain only conjectured because all known liquid metals, like mercury, form Cooper pairs below their solidification temperature[3,4]. Experiments that bypass the constraints imposed by thermodynamic equilibrium are crucial to accessing the forbidden parts of a system's phase space that may host unrealized states[5–11].

Primarily because of intervening phase transitions in candidate materials, a liquid charge density wave (CDW) is one such state that has yet to be experimentally realized despite being speculated about for more than three decades[12,13]. A liquid CDW is distinct from an electronic Fermi liquid, as it possesses a finite order parameter amplitude with a corresponding local periodicity, but nonetheless lacks long-range orientational and translational order. If observed, a liquid CDW would represent a new state of electronic matter and serve as a basis for discovering new classes of electronic liquid crystals. Liquid-like CDWs have been theoretically predicted to play a fundamental role in the anomalous normal-state properties of several families of unconventional superconductors including cuprates, transition metal dichalcogenides and kagome metals, as well as in the electronic properties of various quantum Hall systems[14–24].

However, whether liquid CDWs can exist, even in principle, is controversial. Liquids possess both continuous translational and rotational symmetries, whereas a CDW necessarily resides within the periodic and anisotropic environments of a host crystal. The complete suppression of orientational order may be hampered due to the underlying interaction between the CDW and ionic lattice. In two dimensions, however, the melting transition proceeds through the proliferation of topological defects, as described in the Kosterlitz–Thouless–Halperin–Nelson–Young (KTHNY) theory, and might allow for a liquid CDW even in the presence of a crystalline background[25–27].

Within the KTHNY framework, the solid-to-liquid phase transition evolves in two steps through an intermediate hexatic phase. Hexatics

[1]Department of Physics and Astronomy, University of California Los Angeles, Los Angeles, CA, USA. [2]Department of Physics, Drexel University, Philadelphia, PA, USA. [3]These authors contributed equally: Joshua S. H. Lee, Thomas M. Sutter. e-mail: anshulkogar@physics.ucla.edu

https://doi.org/10.1038/s41567-025-03108-z

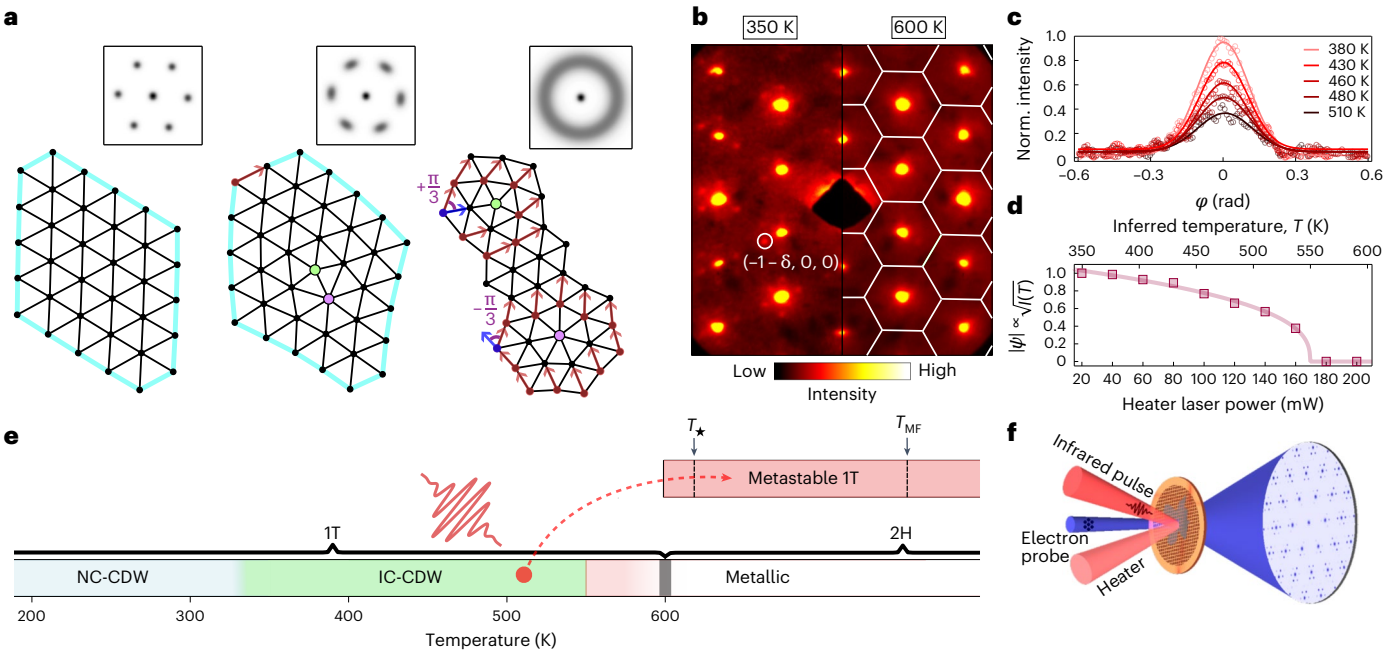

Fig. 1 | Defect-mediated melting of a 2D triangular lattice. a, Schematic of the solid–hexatic–liquid phase transition of a triangular 2D lattice. The insets show diffraction patterns corresponding to each real-space lattice. In the solid state (left), the blue path indicates that the Burgers vector is zero. In the hexatic state (middle), the red arrow indicates the Burgers vector for a path that encloses a single dislocation. In the liquid state (right), the blue arrows illustrate that the Frank angle is +π/3 (−π/3) when transporting a vector around an isolated disclination with five (seven) nearest-neighbour lattice sites. **b**, Static electron diffraction patterns showing the IC-CDW phase at $T = 350$ K (left) and at $T = 600$ K (right). Brillouin-zone outlines are shown overlaid on the $T = 600$ K diffraction pattern. **c**, Representative azimuthal profiles of the $(-1-\delta, 0, 0)$ IC-CDW peak (as indicated in **b**) at selected temperatures. The peak width remains resolution limited through the entire transition. **d**, Measurement of the order parameter $|\psi| \propto \sqrt{I(T)}$ of the IC-CDW-to-metallic transition, where $I(T)$ is the intensity of the $(-1-\delta, 0, 0)$ CDW peak. Through measurements of the heater laser power needed to induce the NC-CDW-to-IC-CDW and IC-CDW-to-metallic transitions, a conversion between the power and sample temperature is inferred. The solid line is a fit to $|\psi| \approx (T_c - T)^{\beta}$ with the extracted critical exponent $\beta = 0.37 \pm 0.04$. **e**, Phase diagram of 1T-TaS_2 as a function of temperature. Above 600 K, 1T-TaS_2 undergoes an irreversible, discontinuous phase transition to the 2H structure, which does not host an IC-CDW phase. However, the application of a femtosecond light pulse can be used to circumvent this transition, allowing for the transient study of a metastable 1T structure that is otherwise inaccessible in equilibrium. **f**, Schematic of the experimental setup showing the probe electron pulse (blue), the pump pulse (red) and the external heater laser (pink).

are characterized by the unbinding of dislocation pairs, which results in the absence of long-range translational order but the retention of quasi-long-range orientational order. Translational and rotational symmetries are ultimately restored in the liquid state through the dissociation of dislocations into individual disclinations/anti-disclinations, which are topological defects that twist the crystal lattice. In a scattering experiment, the hexatic state is marked by a preferential broadening of the diffraction peaks along the azimuthal direction. In the liquid state, the peaks completely broaden into an isotropic diffuse ring of intensity, reflecting the complete loss of long-range orientational order (Fig. 1a). Solid–hexatic–liquid transitions in two dimensions have been investigated in various systems that do not, or only weakly, interact with an underlying lattice. Examples include colloidal crystals[28,29], superconducting vortex lattices[30–32], liquid crystals[33,34], rotating Bose–Einstein condensates[35], skyrmion lattices[36] and Wigner crystallized free electrons on the surface of liquid helium[37,38]. Although previous experiments on CDW materials have uncovered a hexatic state[12,39,40], it remains unclear whether disclinations can unbind to completely remove orientational order.

One of the most promising candidate liquid CDW materials is the transition metal dichalcogenide 1T-TaS_2, in which the CDW is largely two dimensional (2D) with only a weak out-of-plane coupling. Three CDWs undergo a concurrent instability, known as a triple-**q** CDW, which maintains the triangular lattice motif characteristic of the KTHNY theory. Historically, a dislocation-induced hexatic state was observed in 1T-TaS_2 through the substitution of niobium into the tantalum site[12]. Recently, the hexatic state was observed in pristine, minimally disordered 1T-TaS_2 both on photoexcitation and endotaxial stabilization[39,40]; these latter studies provide a renewed impetus and a route to search for the CDW liquid.

A major obstacle in 1T-TaS_2, however, stems from an irreversible, discontinuous phase transition from the 1T to 2H structure that occurs at around 600 K (ref. 41). In a quasi-2D compound like 1T-TaS_2, the metallic-to-incommensurate-CDW (IC-CDW) transition at T_{CDW} (550 K) occurs via a two-to-three-dimensional crossover[42]. Below the mean-field transition temperature, T_{MF} ($\gg T_{CDW}$), 2D correlations begin to build up; three-dimensional correlations emerge only below a temperature T^*, where the interplane correlation length exceeds the interplane distance. Between T^* and T_{MF}, the KTHNY scenario should be applicable, as the system effectively functions as a stack of independent 2D CDW layers. However, both estimated temperature scales, $T^* \approx 630$ K and $T_{MF} \approx 750$ K, lie above the 1T-to-2H polytypic phase transition temperature in a regime that cannot be accessed in thermal equilibrium. Below, we show that ultrafast electron diffraction (UED) can reveal the CDW correlations in this layer-decoupled regime by transiently maintaining the 1T structure in a non-equilibrium, thermally disfavoured state.

We first characterize the incommensurate-CDW-to-metallic phase transition in equilibrium by obtaining static electron diffraction patterns. All the diffraction measurements are performed in a transmission geometry perpendicular to the layers so that the $(HK0)$ plane is experimentally captured. Here (HKL) denote the Miller indices. We extract the temperature dependence of the order parameter $|\psi| \propto \sqrt{I(T)}$, where $I(T)$ is the CDW peak intensity, by increasing the power of a heater laser

https://doi.org/10.1038/s41567-025-03108-z

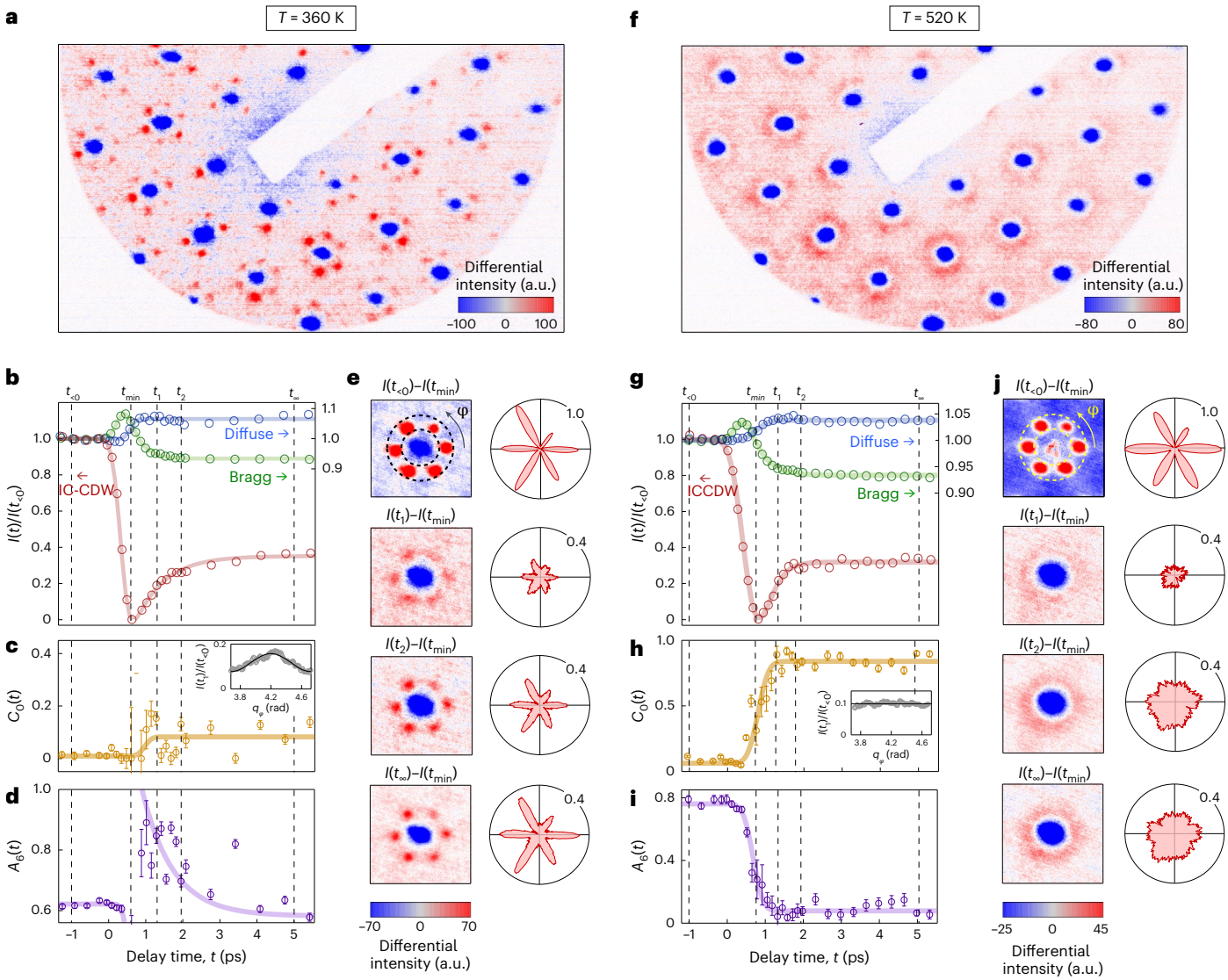

Fig. 2 | Emergence of hexatic and liquid CDW states following a light-induced suppression of the equilibrium order. a, Full differential diffraction pattern with respect to t_{min}. **b**, Temporal dynamics of the integrated intensities of the IC-CDW peaks (red), Bragg peaks (green) and thermal diffuse background (blue) after photoexcitation, at an initial temperature of $T = 360$ K. Several representative time points are labelled: before photoexcitation ($t_{<0}$), at complete suppression of the CDW order (t_{min}) and at (0.5, 1.05, 4.25) ps after t_{min} (t_1, t_2, t_∞). **c**, Time evolution of the offset term $C_0(t)$, representing how much the nodes have lifted in the azimuthal polar plots. The inset shows the azimuthal IC-CDW profile of the $(-1-\delta, 0, 0)$ peak overlaid with $(I(t_1)/I(t_{<0}))\cos(6\phi)$, showing excellent agreement. **d**, Time evolution of the fundamental 6ϕ Fourier coefficient $A_6(t)$. The error bars in **c** and **d** denote one standard deviation in the Fourier decomposition fits. **e**, Differential diffraction profiles at ($t_{<0}$, t_1, t_2, t_∞) with respect to t_{min} (left) and their respective azimuthal polar plots (right). In the polar plots, the contribution of the thermal diffuse background has been subtracted from the overall IC-CDW intensity. **f**–**j**, Same data as in **a**–**e**, but at an initial temperature of $T = 520$ K. The inset in **h** is the same as that in **c** but overlaid with a constant line, showing minimal intensity variations. The azimuthal polar plots in **j** after $t = t_{min}$ show an isotropic structure, a signature of a liquid CDW state.

(Fig. 1 and Methods). Through measurements of the laser power needed to induce the nearly commensurate-to-incommensurate (NC-to-IC) CDW transition at 350 K (ref. 43) and the IC-CDW-to-metallic transition at 550 K (ref. 44), we estimate the change in temperature of our sample induced by the external heater laser (Fig. 1d). An azimuthal cut of the $(-1-\delta, 0, 0)$ peak is displayed in Fig. 1c, which shows the intensity of the CDW peak decreasing as the transition temperature is approached. Broadening of the peaks beyond the momentum resolution of our instrument along both azimuthal and radial directions is not detected within the temperature range investigated (Fig. 1c and Supplementary Notes I–III).

To transiently access the layer-decoupled regime (which would correspond to $T^* < T < T_{MF}$ at thermal equilibrium), we investigate the IC-CDW-to-metallic transition on photoexcitation with 840-nm, 180-fs light pulses at an incident fluence of 6 mJ cm^{-2} (Fig. 2). Pulsed photoexcitation allows for the sample to only be transiently heated and for the CDW to be melted non-thermally; the process by which the CDW recrystallizes can then be investigated as a function of time. Figure 2b,g shows the temporal evolution of the integrated intensity of the IC-CDW satellite peaks, the main Bragg peaks and the change in diffuse background following photoexcitation at 360 K and 520 K, respectively (an estimate of the temperature before photoexcitation is obtained by comparing the intensity of the $(-1-\delta, 0, 0)$ CDW peak at time $t = t_{<0}$ with its equilibrium intensity; Supplementary Note IV). Following photoexcitation, the IC-CDW peak intensity is suppressed within a characteristic timescale of 375 fs and reaches zero by $t = t_{min} \approx 750$ fs, values which are limited by the temporal resolution of our instrument[45]. Over the subsequent picosecond, the system reaches a quasi-equilibrium state. In this state, the CDW peaks only

https://doi.org/10.1038/s41567-025-03108-z

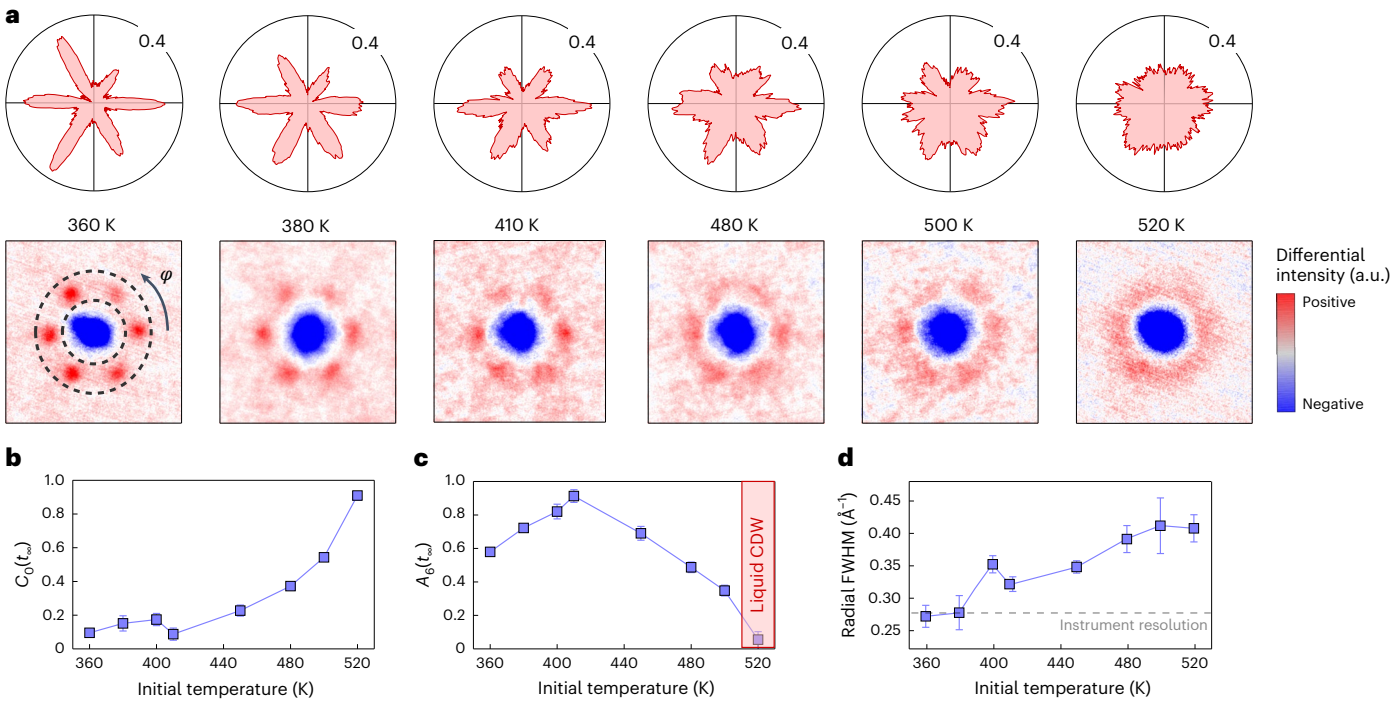

Fig. 3 | Evolution of solid, hexatic and liquid CDW states in the quasi-thermal regime. a, Changes in diffraction intensity $I(t_\infty) - I(t_{min})$ for various initial temperatures (bottom), and their respective azimuthal polar plots at the IC-CDW wavevector (top) after diffuse background subtraction. **b**, Progression of the offset term $C_0(t_\infty)$ once the system has reached a quasi-equilibrium state, as a function of the initial sample temperature. **c**, Progression of the fundamental 6ϕ Fourier coefficient $A_6(t_\infty)$ as a function of initial temperature. The error bars in **b** and **c**, if larger than the symbol size, denote one standard deviation in the Fourier decomposition fits. **d**, Progression of the FWHM of the IC-CDW peaks along the radial direction. The momentum resolution of our instrument is plotted in grey for reference. The error bars denote one standard deviation in the radial fits.

partially recover their original intensity, as the heat incurred from photoexcitation has not diffused out of the illuminated region within the measured time window. An increase in the Bragg peak intensity occurs concurrently with the suppression of CDW peak intensity, a consequence of the elastic scattering sum rule. The subsequent loss of Bragg peak intensity and increase in the diffuse scattering signal arises due to lattice heating through the Debye–Waller effect and the thermal occupation of phonons, respectively (Supplementary Note XI). A number of other CDW systems have been observed to abide by a similar experimental phenomenology, although with different timescales[46–50].

To investigate the changes in orientational and translational order of the CDW during the recovery time frame, we examine changes to the superlattice peak profiles along the azimuthal and radial directions between t_{min} and t_∞ (Fig. 2e,j and Supplementary Video 1). All the presented differential diffraction profiles are averaged over the visible {200} and {110} families of CDW peaks, as well as over several time points, for improved signal-to-noise ratio (Supplementary Note VI). To analyse the orientational order, we perform a Fourier decomposition of the azimuthal CDW intensity profiles and study the dynamics of its coefficients after photoexcitation. The intensity can be expressed as a constant offset in addition to a Fourier series with harmonics of period six (Supplementary Note XII):

$$I_{norm}(\phi, t) = C_0(t) + \sum_{n=1}^{4} A_{6n}(t)\cos(6n\phi), \quad (1)$$

where ϕ denotes the azimuthal angle around the ring shown in Fig. 2e,j (top). Considering the momentum resolution of our instrument, harmonics higher than $n = 4$ provide minimal improvements to the fit and are, thus, excluded. By construction, the sum of the Fourier coefficients equals one at all times (that is, $C_0(t) + \sum_{n=1}^{4} A_{6n}(t) = 1$). The offset term $C_0(t)$ quantifies how much the nodes lift in the polar plot visualization (Fig. 2e,j, right). Importantly, in the raw data, the nodes can lift due to enhanced diffuse scattering present at all momenta in addition to an isotropic scattering component at the CDW wavevector. Therefore, when plotting the Fourier coefficients and polar intensity traces (Figs. 2 and 3), the intensity contributed by the diffuse background is subtracted (that is, $C_0(t)$ quantifies the isotropic intensity component relevant to the CDW dynamics; Supplementary Note VII).

At 360 K, as the CDW recrystallizes after photoexcitation, the peaks substantially broaden along both azimuthal and radial directions (Fig. 2e and Supplementary Fig. 9). At $t = t_1 \approx 1.2$ ps, the peaks can be fit solely with the fundamental 6ϕ Fourier component such that $A_6 \approx 1$ (Fig. 2c,d, inset). Such broadening shows that although the long-range translational order is lost, quasi-long-range orientational order is still present in the CDW superlattice. As shown in a previous work, this hexatic state occurs in the layer-decoupled regime in which only a 2D CDW order is present, and occurs in accordance with the unbinding of dislocation/anti-dislocation pairs[40]. Over the next 2 ps, the A_6 coefficient decreases substantially, whereas the higher-harmonic coefficients increase—observations that are indicative of peak narrowing in the azimuthal direction (Fig. 2d and Supplementary Fig. 11). By $t = t_\infty$, the azimuthal and radial widths of the CDW peaks return to their values before photoexcitation ($t = t_{<0}$) and their intensities have stabilized; the system has largely restored the translationally and orientationally ordered state of the CDW superlattice (Fig. 2a). Together, these data demonstrate that the recovery of the CDW superlattice follows a non-thermal pathway through an intermediate hexatic state.

To observe the liquid CDW state, we repeat the experiment with identical pump parameters but at an initial temperature of 520 K. Although the evolution of the intensities of the CDW peaks, the main Bragg peaks and the diffuse background is similar to those at 360 K, the CDW peak dynamics along the azimuthal direction are noticeably

https://doi.org/10.1038/s41567-025-03108-z

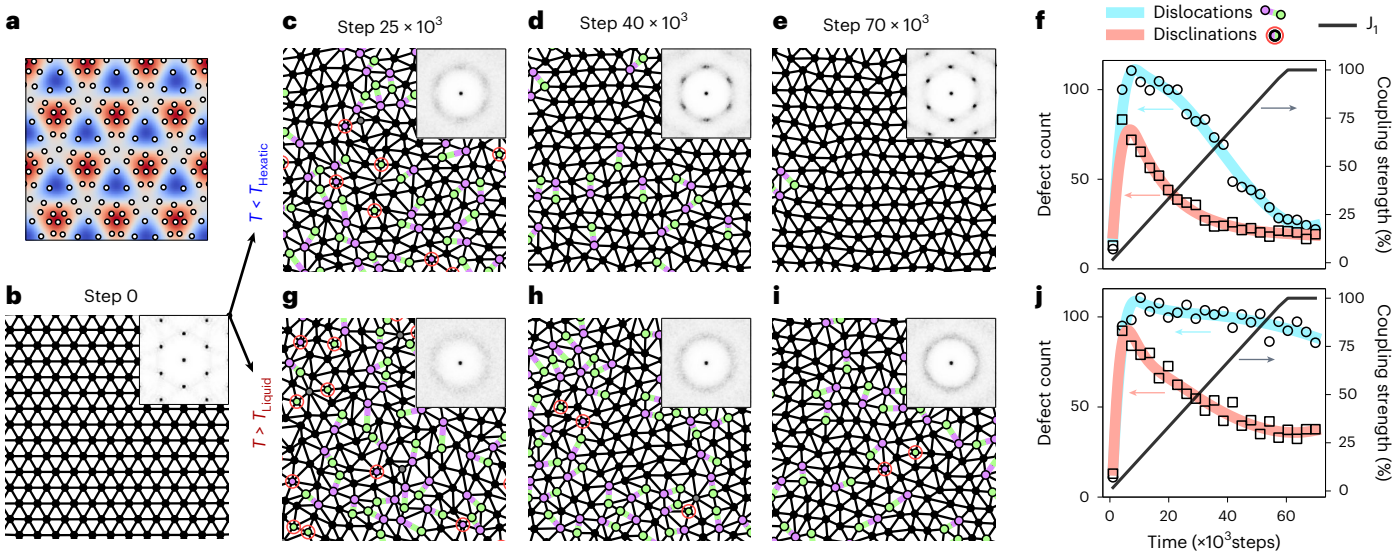

Fig. 4 | Molecular dynamics simulation of a solid–liquid–hexatic transition with quenched interaction strength. a, Schematic of IC-CDW with white-filled points indicating tantalum atoms and the colour map showing the coarse-grained charge density. **b**, Initial state of the 2D molecular dynamics simulation. **c**–**e**, Simulation snapshots at a temperature below the hexatic transition. The black lines show the Delaunay triangulation with defect sites in green (five sites) and purple (seven sites). The disclinations are circled in red. The insets are simulated diffraction patterns. **f**, Number of dislocations (blue curve) and disclinations (red curve) as a function of time. The solid black line shows J_1 ramping back to 100% strength. **g**–**j**, Simulation results at a temperature above the liquid transition.

different (Fig. 2j and Supplementary Video 1). For all the measured times after t_{min}, an isotropic ring of intensity distinct from the diffuse background is visible at the CDW wavevector (Fig. 2f,j). Therefore, $C_0 \approx 1$ between t_1 and t_∞ (partial rings are visible around the lower-order Bragg peaks in Fig. 2f due to effects related to the geometric structure factor, which also affect the CDW peak intensities in Fig. 2a). An azimuthal cut showing minimal intensity variation at the CDW wavevector is displayed in Fig. 2h (inset). The diffuse CDW ring also exhibits persistent radial broadening out to $t = t_\infty$, in stark contrast to the recovery at 360 K, which only exhibited radial broadening for a short time after t_{min} (Supplementary Fig. 9). The isotropic ring of intensity and radial broadening is a signature of the complete loss of both translational and orientational orders of the CDW superlattice. These data are suggestive that the dislocation-type defects have dissociated into unbound disclination pairs. By circumventing the 1T-to-2H transition through photoexcitation, we are, thus, able to observe a liquid CDW state that is otherwise inaccessible in thermal equilibrium.

Together, these data indicate that there are two distinct regimes of physical behaviour. In the quench regime at short timescales ($t \lesssim t_2$), the system is still evolving and has yet to reach a thermalized state. Though relevant, thermal fluctuations in this regime do not dominate the behaviour of the system. Conversely, in the quasi-thermal regime at longer timescales ($t \approx t_\infty \gg t_2$), the absorbed photons have effectively heated the illuminated region, and the system no longer changes with time. At the fluence used in these measurements (6 mJ cm^{-2}), the temperature at $t = t_\infty$ is raised by about 160 K compared with the temperature before photoexcitation (Supplementary Note V). Therefore, for the data taken at initial temperatures of 360 K and 520 K, the final quasi-equilibrium temperatures, $T(t_\infty)$, are approximately 520 K and 680 K, respectively. Importantly, the latter final temperature is above both T_{CDW} and the 1T-to-2H transition temperature, which highlights how transiently heating the system maintains a superheated 1T structure. Below, we show that there are two distinct phase transition pathways towards observing the CDW liquid—a thermal one and a non-thermal one.

We first show how the system thermally evolves from a solid to a liquid at $t = t_\infty$ at various initial temperatures between 360 K and 520 K (Fig. 3a). For initial temperatures within the range of 380 K < T < 410 K, the system gradually progresses from the solid CDW state to the hexatic state, as $A_6(t_\infty)$ begins to increase and the peaks broaden radially (Fig. 3c,d). By 410 K, $A_6(t_\infty) \approx 1$, and dislocation pairs have unbound to destroy the quasi-long-range translational symmetry of the CDW. Above 440 K, $C_0(t_\infty)$ starts to increase substantially, which is indicative of disclination pair unbinding, and at 520 K, the liquid CDW state becomes stabilized as $C_0(t_\infty) \approx 1$ ($A_6(t_\infty)$ decreases in this regime because the Fourier coefficients sum to one). The radial peak width remains relatively constant after its initial rise near T = 410 K, consistent with the fact that both hexatic and liquid CDW states possess only short-range translational order. Taken together, the evolution of the CDW as a function of the background temperature is reminiscent of that predicted by the KTHNY theory. Although further experiments will be needed to verify whether the three dimensionality of the solid precludes the observation of the universal jumps predicted by the theory, the experimental phenomenology is nonetheless in good qualitative agreement with a two-step thermal phase transition through an intermediate hexatic state. Using an ultrafast heating protocol and transiently maintaining a superheated 1T structure, thus, represents the first pathway to observe the CDW liquid.

The non-equilibrium dynamics in the quench regime ($t \lesssim t_2$) represent a second pathway towards the CDW liquid. To understand how the transition proceeds in the quench regime, we perform a 2D molecular dynamics simulation in the presence of the two main forces between particles: (1) a repulsive, Yukawa-type force that is scaled by coupling constant J_1 and (2) an orientational force that models the interaction with the background lattice. The particles in the simulation represent the charge centres of the CDW (Fig. 4a,b). Simulations are initialized in the ordered CDW state (Fig. 4b), and to model the quench, the Yukawa coupling, J_1, is set to zero and linearly ramped back to 100% strength. J_1 is quenched in the simulation because its magnitude, which is proportional to the square of the order parameter, rapidly changes in the experiment as the CDW amplitude is suppressed to zero on photoexcitation. The effect of temperature in the simulations is incorporated through a Langevin noise term acting on all particles with a variance proportional to the simulation temperature. A full description of the 2D molecular dynamics simulation is provided in Supplementary Note XIII.

Snapshots of the simulations are shown for temperatures below the hexatic ordering temperature and above the liquid transition temperature (Fig. 4c–e,g–i). For $T < T_{Hexatic}$, the system progresses from

a solid to a hexatic and back to a solid as a function of time, which reproduces the experimental dynamics observed at 360 K. For the higher-temperature simulation ($T > T_{Liquid}$), the system remains as a liquid indefinitely following the quench, as is observed in the experiment at 520 K. Though tuned by the coupling constant J_1 instead of temperature, the transition similarly proceeds though the proliferation of topological defects. Figure 4f,j shows the number of dislocations and disclinations as a function of time (in terms of simulation steps) for $T < T_{Hexatic}$ and $T > T_{Liquid}$. In the former case, the defects eventually vanish at long times, whereas both disclinations and dislocations persist in the latter. These simulations highlight the crucial role played by topological defects in the formation of the non-equilibrium CDW hexatic and liquid states through the quenching of a non-thermal parameter, which suggests that the quantum Kibble–Zurek mechanism may be operative in this regime[51–53]. Optical quenching, thus, presents a second pathway through which the CDW liquid can be observed.

Our work highlights how light pulses can be used to observe phases of matter that are hidden by intervening phase transitions. CDW recrystallization in 1T-TaS_2 is revealed to proceed via liquid and hexatic CDW phases through two distinct pathways. Liquid CDWs, in particular, represent a new state of matter that may be prevalent, but have so far eluded detection, in a number of correlated electron systems. Whether the liquid CDW can be quenched into an amorphous glassy state, novel forms of liquid crystalline CDWs or other electronically textured phases remains to be seen, but present interesting avenues for further exploration. Ultimately, our work paves the way towards the discovery of exotic phases of electronic matter using non-equilibrium methods that can access regions of phase diagrams that may otherwise remain thermally forbidden.

Online content

Any methods, additional references, Nature Portfolio reporting summaries, source data, extended data, supplementary information, acknowledgements, peer review information; details of author contributions and competing interests; and statements of data and code availability are available at https://doi.org/10.1038/s41567-025-03108-z.

References

1. Anderson, M. H. et al. Observation of Bose-Einstein condensation in a dilute atomic vapor. *Science* **269**, 198–201 (1995).
2. Davis, K. B. et al. Bose-Einstein condensation in a gas of sodium atoms. *Phys. Rev. Lett.* **75**, 3969–3973 (1995).
3. Tenney, C. M., Croft, Z. F. & McMahon, J. M. Metallic hydrogen: a liquid superconductor? *J. Phys. Chem. C* **125**, 23349–23355 (2021).
4. Leggett, A. J. in *PWA90: A Lifetime of Emergence* (eds Chandra, P., Coleman, P., Kotliar, G., Ong, P., Stein, D. L. & Yu, C.) 97–103 (World Scientific, 2016).
5. Stojchevska, L. et al. Ultrafast switching to a stable hidden quantum state in an electronic crystal. *Science* **344**, 177–180 (2014).
6. Kogar, A. et al. Light-induced charge density wave in $LaTe_3$. *Nat. Phys.* **16**, 159–163 (2020).
7. Fausti, D. et al. Light-induced superconductivity in a stripe-ordered cuprate. *Science* **331**, 189–191 (2011).
8. Disa, A. S. et al. Photo-induced high-temperature ferromagnetism in $YTiO_3$. *Nature* **617**, 73–78 (2023).
9. Mitrano, M. et al. Possible light-induced superconductivity in K_3C_{60} at high temperature. *Nature* **530**, 461–464 (2016).
10. Nova, T. F. et al. Metastable ferroelectricity in optically strained $SrTiO_3$. *Science* **364**, 1075–1079 (2019).
11. Li, X. et al. Terahertz field–induced ferroelectricity in quantum paraelectric $SrTiO_3$. *Science* **364**, 1079–1082 (2019).
12. Dai, H. & Lieber, C. M. Solid-hexatic-liquid phases in two-dimensional charge-density waves. *Phys. Rev. Lett.* **69**, 1576–1579 (1992).
13. Dai, H., Chen, H. & Lieber, C. M. Weak pinning and hexatic order in a doped two-dimensional charge-density-wave system. *Phys. Rev. Lett.* **66**, 3183 (1991).
14. Hayden, S. M. & Tranquada, J. M. Charge correlations in cuprate superconductors. *Annu. Rev. Condens. Matter Phys.* **15**, 215 (2024).
15. Subires, D. et al. Frustrated charge density wave and quasi-long-range bond-orientational order in the magnetic kagome FeGe. *Nat. Commun.* **16**, 4091 (2025).
16. Kivelson, S. A., Fradkin, E. & Emery, V. J. Electronic liquid-crystal phases of a doped Mott insulator. *Nature* **393**, 550–553 (1998).
17. Delacrétaz, L. V. et al. Theory of hydrodynamic transport in fluctuating electronic charge density wave states. *Phys. Rev. B* **96**, 195128 (2017).
18. Taraphder, A. et al. Preformed excitonic liquid route to a charge density wave in 2H-$TaSe_2$. *Phys. Rev. Lett.* **106**, 236405 (2011).
19. Snow, C. S. et al. Quantum melting of the charge-density-wave state in 1T-$TiSe_2$. *Phys. Rev. Lett.* **91**, 136402 (2003).
20. Ciftja, O., Lapilli, C. M. & Wexler, C. Liquid crystalline states for two-dimensional electrons in strong magnetic fields. *Phys. Rev. B* **69**, 125320 (2004).
21. Wexler, C. & Ciftja, O. Liquid crystalline states in quantum Hall systems. *J. Phys.: Condens. Matter* **14**, 3705 (2002).
22. Fradkin, E. & Kivelson, S. A. Liquid-crystal phases of quantum Hall systems. *Phys. Rev. B* **59**, 8065 (1999).
23. Nie, L., Tarjus, G. & Kivelson, S. A. Quenched disorder and vestigial nematicity in the pseudogap regime of the cuprates. *Proc. Natl Acad. Sci. USA* **111**, 7980–7985 (2014).
24. Milward, G. C., Calderón, M. J. & Littlewood, P. B. Electronically soft phases in manganites. *Nature* **433**, 607–610 (2005).
25. Nelson, D. R. & Halperin, B. I. Dislocation-mediated melting in two dimensions. *Phys. Rev. B* **19**, 2457–2484 (1979).
26. Halperin, B. I. & Nelson, D. R. Theory of two-dimensional melting. *Phys. Rev. Lett.* **41**, 121–124 (1978).
27. Kosterlitz, J. M. Kosterlitz–Thouless physics: a review of key issues. *Rep. Prog. Phys.* **79**, 026001 (2016).
28. Keim, P., Maret, G. & von Grünberg, H. H. Frank's constant in the hexatic phase. *Phys. Rev. E* **75**, 031402 (2007).
29. Kusner, R. E. et al. Two-stage melting of a two-dimensional collodial lattice with dipole interactions. *Phys. Rev. Lett.* **73**, 3113–3116 (1994).
30. Troyanovski, A. M. et al. STM imaging of flux line arrangements in the peak effect regime. *Phys. Rev. Lett.* **89**, 147006 (2002).
31. Guillamón, I. et al. Direct observation of melting in a two-dimensional superconducting vortex lattice. *Nat. Phys.* **5**, 651–655 (2009).
32. Roy, I. et al. Melting of the vortex lattice through intermediate hexatic fluid in an *a*-MoGe thin film. *Phys. Rev. Lett.* **122**, 047001 (2019).
33. Brock, J. D. et al. Orientational and positional order in a tilted hexatic liquid-crystal phase. *Phys. Rev. Lett.* **57**, 98–101 (1986).
34. Cheng, M. et al. Observation of two-dimensional hexatic behavior in free-standing liquid-crystal thin films. *Phys. Rev. Lett.* **61**, 550–553 (1988).
35. Sharma, R. et al. Thermal melting of a vortex lattice in a quasi two-dimensional Bose gas. *Phys. Rev. Lett.* **133**, 143401 (2024).
36. Huang, P. et al. Melting of a skyrmion lattice to a skyrmion liquid via a hexatic phase. *Nat. Nanotechnol.* **15**, 761–767 (2020).
37. Gallet, F. et al. Fluctuations and shear modulus of a classical two-dimensional electron solid: experiment. *Phys. Rev. Lett.* **49**, 212–215 (1982).
38. Knighton, T. et al. Evidence of two-stage melting of Wigner solids. *Phys. Rev. B* **97**, 085135 (2018).
39. Sung, S. H. et al. Endotaxial stabilization of 2D charge density waves with long-range order. *Nat. Commun.* **15**, 1403 (2024).

40. Domröse, T. et al. Light-induced hexatic state in a layered quantum material. *Nat. Mater.* **22**, 1345–1351 (2023).
41. Givens, F. L. & Fredericks, G. E. Thermal expansion op $NbSe_2$ and TaS_2. *J. Phys. Chem. Solids* **38**, 1363–1365 (1977).
42. Gruner, G. *Density Waves in Solids* (CRC Press, 2018).
43. Thomson, R. E. et al. Local charge-density-wave structure in 1T-TaS_2 determined by scanning tunneling microscopy. *Phys. Rev. B* **38**, 10734–10743 (1988).
44. Rossnagel, K. On the origin of charge-density waves in select layered transition-metal dichalcogenides. *J. Phys.: Condens. Matter* **23**, 213001 (2011).
45. Sutter, T. M. et al. Vector-based feedback of continuous wave radiofrequency compression cavity for ultrafast electron diffraction. *Struct. Dyn.* **11**, 024303 (2024).
46. Zong, A. et al. Evidence for topological defects in a photoinduced phase transition. *Nat. Phys.* **15**, 27–31 (2019).
47. Cheng, Y. et al. Light-induced dimension crossover dictated by excitonic correlations. *Nat. Commun.* **13**, 963 (2022).
48. Gonzalez-Vallejo, I. et al. Time-resolved structural dynamics of the out-of-equilibrium charge density wave phase transition in $GdTe_3$. *Struct. Dyn.* **9**, 014502 (2022).
49. Trigo, M. et al. Coherent order parameter dynamics in $SmTe_3$. *Phys. Rev. B* **99**, 104111 (2019).
50. Han, T. R. T. et al. Structural dynamics of two-dimensional charge-density waves in $CeTe_3$ investigated by ultrafast electron crystallography. *Phys. Rev. B* **86**, 075145 (2012).
51. Zurek, W. H., Dorner, U. & Zoller, P. Dynamics of a quantum phase transition. *Phys. Rev. Lett.* **95**, 105701 (2005).
52. Dziarmaga, J. Dynamics of a quantum phase transition: exact solution of the quantum Ising model. *Phys. Rev. Lett.* **95**, 245701 (2005).
53. Polkovnikov, A. Universal adiabatic dynamics in the vicinity of a quantum critical point. *Phys. Rev. B* **72**, 161201 (2005).

Methods

Crystal growth and sample preparation

Single crystals of 1T-TaS_2 were grown in evacuated quartz ampoules (pressure less than 10 mtorr) in a three-zone gradient temperature furnace (Lindberg/Blue-M) using iodine chemical vapour transport method[54,55]. The starting materials were metal powders of Ta and Ti (purity better than 99.99%; Alfa Aesar), sulfur powder (purity, 99.999%; Puratronic) and iodine transport agent (purity, 99.985%; Puratronic). The stoichiometric ratio of metal and chalcogen powders (with slight excess of chalcogen) along with traces of iodine were loaded in the ampoules and the growth proceeded in a gradient of around 200 °C m^{-1} at 700 °C. The growth was terminated after 14 days with quenching the samples from 700 °C to room temperature to avoid the formation of interpolymorphic transformations. The millimetre-sized crystals have been characterized using structural (X-ray diffraction), spectroscopic (energy-dispersive X-ray spectroscopy to verify stoichiometry) and low-temperature electrical transport probes.

Approximately 60-nm-thick, 250 µm × 250 µm laterally sized flakes of 1T-TaS_2 were sectioned along the a–b plane using an ultramicrotome fitted with a diamond blade. The sectioned flakes were transferred from water onto standard transmission electron microscopy copper mesh grids (90 µm hole widths). The grids are clamped onto our aluminium-based sample-mounting apparatus. Silver-filled, ultrahigh-vacuum-compatible thermal paste was applied to the edges of the copper grids to improve thermal contact between the grid and the sample mount.

Kiloelectronvolt UED with an external heating laser

Experiments on the incommensurate-to-metallic transition in 1T-TaS_2, both in equilibrium and through photoexcitation, were carried out at the University of California, Los Angeles, using our table-top UED apparatus. Photoexcitation (pump) pulses originate from a 1,030-nm (1.20-eV), 180-fs Yb-based regenerative amplifier laser (PHAROS, LIGHT CONVERSION) with tunable repetition rates up to 20 kHz. The pump pulses are directed into an optical parametric amplifier, allowing us to tune the wavelength of the output light pulses to 840 nm (1.48 eV). These pulses are subsequently focused onto a 510 µm × 510 µm (full-width at half-maximum (FWHM)) area on the sample.

The electron pulses are generated by focusing the fourth-harmonic output (257.5 nm, 4.81 eV) of the 1,030-nm light onto a 60 µm × 60 µm (FWHM) area on a polycrystalline copper cathode. The photoexcited electron pulses are then accelerated to 40.4 kV in a d.c. field. To combat temporal broadening due to space-charge effects, the pulses are sent through a radio-frequency cavity to achieve a temporal resolution of 375 fs (FWHM). The compressed electron pulses are focused by a magnetic lens to a 90 µm × 90 µm (FWHM) area on the sample. The diffracted electrons are collected and amplified by a microchannel plate detector with a phosphor screen (Photonis QS24215-1), and the final diffraction pattern is imaged using a complementary metal–oxide–semiconductor sensor camera (FLIR Blackfly S USB3).

In addition to the pump and probe pulses, we use an additional heating laser to adjust the equilibrium temperature of our sample. The heating laser originates from the oscillator output of our ytterbium-doped potassium gadolinium tungstate laser, with a wavelength of 1,030 nm (1.20 eV) and at a repetition rate of 79.33 MHz. The heating laser also operates at a maximum fluence of about 2 µJ cm^{-2}. Due to its low fluence, individual pulses from the heating laser do not have an effect on the observed temporal dynamics after pump photoexcitation, providing only the effect of steady-state heating of the sample.

Data availability

The data that support the findings of this study are provided in the Article. Source data are provided with this paper. These data are also available via Zenodo at https://doi.org/10.5281/zenodo.15453892 (ref. 56). Additional data related to the paper are available from the corresponding author upon request.

Code availability

The code used to produce the figures in this work is available via Zenodo at https://doi.org/10.5281/zenodo.17383782 (ref. 57).

References

54. Di Salvo, F. J. et al. Effects of doping on charge-density waves in layer compounds. *Phys. Rev. B* **12**, 2220 (1975).
55. Di Salvo, F. J. et al. Preparation and properties of a new polytype of tantalum disulfide (4Hb-TaS_2). *J. Phys. Chem. Solids* **34**, 1357–1362 (1973).
56. Lee, J. S. H. Observation of a hidden charge density wave liquid. *Zenodo* https://doi.org/10.5281/zenodo.15453892 (2025).
57. Sutter, T., Lee, J., Karapetrov, G., Musumeci, P. & Kogar, A. Two dimensional molecular dynamics simulation (KTHNY). *Zenodo* https://doi.org/10.5281/zenodo.17383782 (2025).

Acknowledgements

We thank S. E. Brown, R. Bruinsma and X. Zhang for insightful discussions regarding this work. We thank M. Rasiah, S. Wang, J. Higgins, A. Ody and A. Kulkarni for their instrumentation work in the kiloelectronvolt UED setup at University of California, Los Angeles. We acknowledge support from the US Department of Energy, Office of Science, Office of Basic Energy Sciences, under award number DE-SC0023017 (A.K.; data taking, data analysis and manuscript writing). We also acknowledge support from STROBE: a National Science Foundation Science and Technology Center under grant number DMR-1548924 (A.K. and P.M.; instrumentation).

Author contributions

J.S.H.L. and T.M.S. performed the diffraction measurements. J.S.H.L. and T.M.S. prepared the samples for measurements. J.S.H.L. and T.M.S. built the kiloelectronvolt UED beamline at University of California, Los Angeles, under the supervision of A.K. and P.M. G.K. grew the crystals for the experiment. J.S.H.L. performed the data analysis with theoretical input from T.M.S. and A.K. T.M.S. performed the molecular dynamics simulations. J.S.H.L., T.M.S. and A.K. wrote the paper with important input from all other authors. The work was supervised by A.K.

Competing interests

The authors declare no competing interests.

Additional information

Supplementary information The online version contains supplementary material available at https://doi.org/10.1038/s41567-025-03108-z.

Correspondence and requests for materials should be addressed to Anshul Kogar.

Peer review information *Nature Physics* thanks Haiyun Liu, Chih-Wei Luo and the other, anonymous, reviewer(s) for their contribution to the peer review of this work.